Multi-probe Enabled Over-the-air Calibration of Millimeter-wave Antenna Array: Concept and Experimental Validation

Zhang, Fengchun; WANG, ZHENGPENG ; Hong Loh , Tian ; Gui, Yonghao; si, tang; Fan, Wei

Published in:
I E E E Antennas and Propagation Magazine

Publication date:
2024

Multi-probe Enabled Over-the-air Calibration of Millimeter-wave Antenna Array: Concept and Experimental Validation

F. Zhang, Z. Wang, T. Loh, Y. Gui, S. Tang, W. Fan, ***Senior Member, IEEE***

F. Zhang is with the Antennas, Propagation and Millimeter-wave Systems section at the Department of Electronic Systems, Aalborg University, Denmark. T. Loh and Y. Gui are with the Electromagnetic Technologies Group, Electromagnetic & Electrochemical Technologies Department, National Physical laboratory, United Kingdom. S. Tang and Z. Wang are Electronics and Information Engineering, Beihang University, Beijing 100191, China. W. Fan (corresponding author) is with National Mobile Communications Research Laboratory, School of Information Science and Engineering, Southeast University, China.

Manuscript received month March x, 2023; revised month August x, 2023. First published xx xx, 2024. Current version published month xx, 2024.

Abstract: Millimeter wave (mmWave) antenna array systems with high-gain beam-steerable capability play a key role in fulfilling the high data-rate demands of the fifth generation (5G) and beyond wireless technologies. Rigorous array calibration is essential to ensure their radiation performance fulfills the standard requirements before massive rollout. These tests will exclusively transition to over-the-air (OTA) testing approaches with antennas included, due to the lack of antenna connectors and their compact and highly integrated designs in emerging mmWave radio systems. This has posed huge challenges on measurement and calibration of mmWave antenna arrays, due to the more demanding requirement on system complexity, implementation cost, measurement time, and measurement uncertainty. In this work, a multi-probe framework for phased array calibration is introduced, aiming to achieve objectives including measurement range reduction, measurement efficiency improvement and measurement accuracy enhancement compared with the conventional single-probe method. The basic principle, capabilities, limitations, and design of multi-probe configuration are detailed for each measurement objective. Moreover, extensive measurement results were presented to validate the effectiveness and robustness of the proposed multi-probe based array calibration algorithms for each measurement objective.

Index Terms: mmWave phased array, array calibration, over-the-air testing, multi-probe framework, beam-steering antennas.

1. Introduction

Millimeter-wave (mmWave) technology is essential to fulfill the high data-rate demands of current 5G and future wireless communication systems, thanks to its vast available spectrum resource compared to legacy bands (i.e. sub-6 GHz). Due to high transmission loss and susceptibility to blockage in mmWave bands, high-gain and beam-steerable array systems are essential to achieve good signal to noise ratio (SNR) as well as to maintain the link reliability in dynamic propagation environments. Moreover, technology trends in developing highly integrated radio transceiver design will be inevitable in mmWave bands due to cost concerns [1], [2]. This has posed great challenges on their testing and measurement methods, due to its more demanding requirement on system complexity, implementation cost and measurement time. There is an urgent need for practical, fast, accurate and cost-effective solutions for testing integrated mmWave antenna arrays [3]–[6].

Rigorous array calibration is essential to ensure accurate array radiation performance. The objective of calibration is to detect the initial complex excitations in the radio frequency (RF) chains connected to the array elements, and calibrate them out to ensure homogeneous excitation among

RF chains. Compared to legacy frequency bands, the array calibration of mmWave radios becomes more essential due to utilization of active components in the RF channels. Array calibration is generally required for any multi-antenna/channel systems to achieve desired performance. For example, calibrating a plane wave generator (PWG) is crucial to produce a high-quality plane-wave field in the quiet zone [7]. Array calibration has been a long-standing research topic, and many methods have been reported. The RF chain complex responses of individual branches can be directly measured in a conducted manner via removing the antennas and accessing each antenna port with a RF cable, as done in [8]. The conducted method has been dominantly adopted in the industry for the legacy frequency bands, thanks to its simplicity and low-cost. However, due to the highly integrated RF transceiver designs at mmWave and above, antenna connectors for testing purposes will hardly be preserved. Moreover, the number of elements in mmWave phased arrays has grown dramatically due to the higher density packaging enabled by the shorter wavelengths, making conducted testing infeasible. Hence, calibrating phased arrays in a radiated or an over-the-air (OTA) manner, is inevitable, especially for mmWave radios.

In the OTA array calibration, antenna elements of array under test (AUT) are employed as interfaces to transmit or receive plane-waves in its boresight direction. This leads to that calibration coefficients are composed of the responses in the RF chains and boresight radiation patterns of AUT elements. The mmWave antennas with digital, analog and hybrid beamforming architectures have been reported [9], [10]. For arrays with digital beam-forming architectures, signals of individual RF chains can be independently designed, which can greatly simplify the calibration procedure. For example, it was reported in [11] that all RF chains can be simultaneously calibrated by feeding orthogonal signals in individual RF chains, e.g. pseudo-noise (PN) sequences, and the corresponding calibration coefficients can be simultaneously estimated via correlating the received signal with the fed PN sequences. For phased arrays with analog beam-forming architectures, the amplitude and phase tuning is applied to signals in different chains originating from the same RF signal input. The array calibration can be typically conducted with the help of the attenuator and phase shifter setting in the feeding network [12], [13]. The phased arrays with hybrid beam-forming architectures can in principle be calibrated via properly combining the methods for arrays with analog and digital architectures. Sub-array concept has also been widely employed for analog-structured antenna arrays to reduce system complexity and cost, where array elements are grouped into sub-arrays (i.e., a common amplitude and phase tuning link is shared by the elements within the sub-array) and then sub-arrays form the entire array (i.e. individual amplitude and phase tuning link is connected to each sub-array). The sub-array concepts have been widely employed for base station and PWG designs [14], [15]. Array calibration for antenna elements without individual amplitude and phase tuning links, e.g. elements within the sub-array, is very challenging [16], which typically requires reconstruction of field distribution over the array apertures via applying time-consuming and highly demanding field transformation methods [17]–[19].

In this work, we focus on calibration for analog-beamforming type phased arrays with amplitude and phase-toggling ability for each element. To mimic plane-wave impinging at each AUT element, the park-and-probe approach is widely adopted in the industry by moving the probe antenna installed on a mechanical scanner to align with each activated AUT element while de-activating other AUT elements (via setting attenuators) and recording the complex responses for each RF chain sequentially [20], [21]. It was demonstrated that measurement in this “on-off mode” is not preferred for mmWave phased arrays [22] and mechanical movement is rather slow and inaccurate, especially for large-scale arrays. In contrast to the "on-off mode", the "all-on mode" can measure component-to-component non-uniformity with considering non-negligible mutual coupling effects between components. Hence, calibration performed in the "all-on" mode is more accurate for the mmWave phased array [22]. As detailed in Section II, the AUT can be calibrated in the “all-on mode” in the plane-wave condition approximated by the direct-far-field (DFF), compact antenna testing range (CATR) or plane wave generator (PWG) setups [23]. However, the DFF setup requires a large measurement distance, often suffering from link budget issues and demanding chamber requirements. On the other hand, CATR setups can be employed to construct plane-wave field in a distance smaller than the DFF, but the system implementation cost is still high.

Many PWG prototypes have been proposed for base station testing in the sub-6 GHz [14], [24], [25]. However, the applicability of PWGs in mmWave frequency band are not mature yet, mainly due to the limited supported bandwidth and low-resolution of phase shifters and attenuators, though some works have been reported in the literature [7], [26]. Moreover, the DFF, CATR and PWG solutions may become too costly and impractical to realize OTA testing for mmWave radios that employ larger-scale configurations. Besides the system cost, another key challenge is the measurement efficiency, i.e. the minimum required number of measurements for array calibration. For calibrating an AUT composed of N antenna elements, the minimum required number of measurements is N for the complex-signal measurements based methods in [27], [28] and should be at least $2N + 1$ for the power-only measurements based methods as discussed in [29], respectively. Nevertheless, the measurement efficiency is still slow, given that thousands of antennas might be employed in mmWave base stations. Lastly, for phased arrays working in its default beamforming mode (i.e., with simultaneous phase tuning of individual AUT elements according to the beam-steering direction), the array calibration accuracy can be significantly affected by the beam-steering angle range of the AUT [28]. The calibration results are highly susceptible to system uncertainties when the steering angular range is small.

In this paper, a multi-probe framework is introduced to address these key challenges identified for the single-probe setup. The multi-probe framework has been introduced in [30] to reduce the measurement distance (from far-field distance of the AUT to the far-field distance of the AUT element), in [31] to improve the measurement efficiency (by a factor of M, with M being the number of employed probe antennas) and in [32] to improve measurement accuracy for beam-steering phased arrays (by improving the effective beam-steering angular range of the AUT) in our previous works. The key contribution of this paper is to review these algorithms, to unify the multi-probe framework for achieving different objectives, and to present new measurement results to further validate the concept. This paper is organized as follows: Section II explains the single-probe algorithms; Section III describes the proposed multi-probe algorithms; Section IV presents several measurement campaigns in different anechoic chambers to validate the multi-probe framework; and finally, conclusions are drawn in Section V.

2. Boresight plane-wave methods

Calibration coefficients are defined as the RF chain responses when an AUT is illuminated by the boresight plane-waves as illustrated by Fig. 1. The objective is to determine the calibration coefficient vector $\mathbf{c} = \{c_n\} = \{\tilde{c}_n \cdot g_n^o\},\ n \in [1, N]$, with $\tilde{c}_n$ and g_n^o denoting the n-th RF chain response and complex pattern of the n-th AUT element in the boresight direction, respectively.

Supposing the AUT operates in the receiver (Rx) mode, the composite complex field signal vector received by the AUT antennas for the P complex weight settings can be written as:

$$\mathbf{y} = \mathbf{W} \cdot \mathbf{c}. \tag{1}$$

The vector $\mathbf{y} \in \mathbb{C}^{P\times 1}$ represents the complex signal vector received at the output port, with the p-th entry y_p being the measured signal when the p-th set of complex weights is applied. The received signal vector $\mathbf{y}$ can be measured by, e.g., a vector network analyzer (VNA). The matrix $\mathbf{W} \in \mathbb{C}^{P\times N}$ denotes the complex weighting matrix, where each row vector contains a set of weights applied to the AUT elements with $w_{p,n}$ being the p-th set of complex weight implemented to the n-th AUT element. According to (1), $\mathbf{c}$ can be calculated by a pseudo inverse operation.

In practice, phase shifters and attenuators will introduce both amplitude and phase uncertainties in the $\mathbf{W}$. Furthermore, some inherent noise will exist in $\mathbf{y}$ as well. These uncertainties will be amplified and thereby introduce possibly large errors to calibration coefficient vector, if the matrix $\mathbf{W}$ is ill-conditioned (i.e., with a large condition number). Thus, the complex weighting matrix $\mathbf{W}$ should be properly designed to minimize its condition number.

When an AUT is calibrated with the "on-off" method, the weighting matrix $\mathbf{W}$ is an $N \times N$ identity matrix. Since the inverse of an identity matrix is the identity matrix itself, the calibration

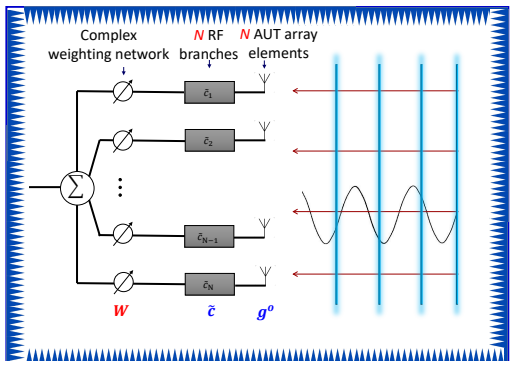

Fig. 1. Calibration system diagram.

vector $\mathbf{c}$ is directly measured. Though this method is simple and straightforward, it is slow and suffers many shortcomings for mmWave radios as discussed [22], [33].

Thus, it is preferable to calibrate the AUT in its default "all-on" mode, i.e., with all AUT elements activated simultaneously. For AUTs calibrated in the "all-on" mode, the state-of-the-art complex-signal and power-only based methods with a single probe far-field setup are discussed below.

2.1. Complex signal methods

The vector $\mathbf{c}$ can be estimated via solving the least squares (LS) equation in (1) for the complex signal methods. Two representative designs of $\mathbf{W}$ are discussed in the literature.

2.1.1. Hadamard matrix based methods [27], [34]

A Hadamard matrix is a square matrix composed of entries of either 1 or -1 and with their rows or columns mutually orthogonal. It is one of the best conditioned matrix structure that gives the minimum condition number 1. Hadamard matrix was proposed as the optimal weighting matrix for phased array calibration in [27]. This solution was further improved in [34] by adding one more measurement to eliminate the accumulated error at the first AUT element when using [27]. The Hadamard matrix based methods, which require only 1-bit phase shifters, are robust to phase shifter uncertainties as well as measurement noise. As discussed in [27], to calibrate an AUT with N elements, the required number of measurements P should be no smaller than N.

2.1.2. Discrete Fourier transform (DFT) matrix based method

A DFT matrix is a best-conditioned matrix (i.e., with the minimum condition number of 1) as well. Since the size of a DFT matrix can be any positive integer number, a minimum number of measurements can always be achieved by setting $P = N$. As discussed in [28], a DFT matrix can be constructed with the beam-steering vectors of a uniform linear array (ULA) as

$$w_{p,n} = e^{-j2\pi(n-1)\cdot\frac{d}{\lambda}\sin\phi_p}, \tag{2}$$

where d represents the element spacing of the ULA, ϕ_p denotes the direction of the p-th beam, and λ denotes the wavelength.

As theoretically derived in [28], in order to construct a complete DFT matrix, the minimum beam-steering range of a ULA should satisfy

$$\Phi_{\text{min}} = \arcsin\left(\frac{P-1}{P}\cdot\frac{\lambda}{2d}\right). \tag{3}$$

The DFT matrix based method is especially useful for calibrating ULAs when the phase shifters of the elements can only work in the default beam-steering mode. It is as robust as the Hadamard matrix based method, due to the same minimum condition number. However, it has also some shortcomings. This method requires phase shifters with a bit number no smaller than $\log_2 N$.

As discussed in [28], the calibration performance degrades as the beam-steering range Φ gets smaller, for $\Phi \leq \Phi_{\text{min}}$. Further, for a non-ULA type AUT, it might be not possible to construct the perfect DFT matrix. As a result, a best-conditioned matrix cannot always be guaranteed.

2.2. Power-only methods

The complex signal methods might not be applicable when the phase measurement is not accessible or inaccurate. This necessitates the calibration methods based on power-only measurements.

2.2.1. The rotating element electric field vector (REV) method [35]

The classic REV method is one of the most widely adopted power-only methods for array calibration. As the name suggested, the phase toggling is implemented successively for AUT elements, namely, one AUT element at a time, where the phase of one AUT element (i.e., the rotated element) is toggled from 0^o to 360^o while keeping phases of other AUT elements to 0^o. Based on the recorded power-only data associated to the phase toggling operated to a given AUT element, the calibration coefficient of this rotated element normalized by the composite coefficients of all AUT elements can be extracted as detailed in [35]. One major drawback of this method is the measurement efficiency, where $Q \times N$ measurements are required with Q denoting the number of phase states set for the rotated elements.

2.2.2. Fast amplitude-only methods

In order to speed up the calibration procedure, several algorithms have been proposed to reduce the number of phase states set for the rotated elements [12], [29], [36], [37], where the method in [29] achieves the minimum required measurements (i.e., $2N + 1$ measurements) in theory. However, an inevitable consequence caused by the reduced number of measurements is the less accurate and robust calibration results compared to the classic REV method, which typically requires more phase states set for the rotated elements.

2.3. Discussion

The discussed calibration methods generally assume plane-wave testing condition, which suffer from the following drawbacks:

- A high-quality plane-wave field illuminating the AUT is required. For AUTs with large electrical apertures operating in mmWave bands, such requirement will be very challenging for the DFF setup due to large measurement distance requirement. As discussed, the CATR and PWG setups are also costly and will not be scalable for future mmWave radios.
- Many mmWave radios can only work in the default beam-steering mode with a limited steering angular range. According to (3), the calibration might suffer from large errors.
- The minimum number of complex-signal measurements for calibrating an N-element AUT is N, which might be problematic for the AUTs with a large number of elements.

To tackle the above challenges related to measurement setup range (and associated cost), measurement accuracy and efficiency, a multi-probe framework is discussed in this paper. Note that the discussion in this paper is limited to complex-signal based methods, while the multi-probe concept will be extended to power-only based methods in our future work.

3. Multi-probe enabled array calibration

The diagram of a multi-probe setup is depicted in Fig. 2, where M probe antennas are employed. In the following, the multi-probe scheme in two application scenarios are discussed: 1) multi-probe far-field setup with the purpose to improve the measurement accuracy or the measurement efficiency for beam-steering AUT, and 2) the multi-probe near-field setup to reduce the required measurement distance. In the far-field setup, plane-waves impinging from probe directions to the AUT is assumed. In the near-field setup, the probes are located in the near-field region of the AUT, but in the far-field region of the AUT element. Note that this region is also termed as "mid-field" in

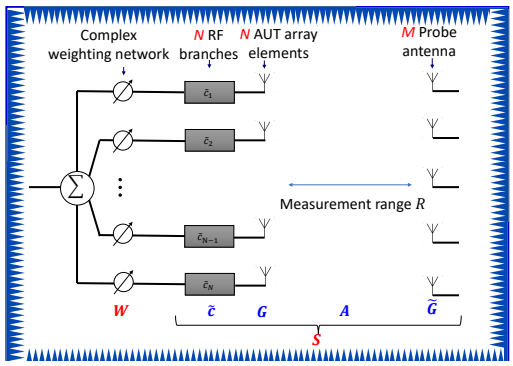

Fig. 2. Calibration system diagram of a multi-probe setup.

some works [3], [38]. The multi-probe scheme can be realized by moving a single probe antenna to predefined locations (i.e., virtual probe array concept) or using multiple probe antennas directly. Note that multi-reflector compact range (to generate plane waves of different impinging angles) or multi-PWG [39], [40] can be seen as multi-probe scheme in a far-field setup as well. For simplicity, we assume the probe antennas are successively activated, namely, in an on-off manner.

3.1. Multi-probe far-field setup

The principle is that the array factors associated with the multi-probe locations can be converted into the beam-steering factors of the array, which can be used to effectively widen the beam-steering angular range with the sparsely distributed probes [32] and furthermore speed up the calibration procedure due to the fewer phase settings in the feeding network [31]. The discussion on the multi-probe far-field setup is focused on the calibration of the ULA-type AUT.

In the multi-probe far-field setup, the probes are placed along a circle, whose center is aligned with the AUT center and radius is set to R. The multi-probe antennas are oriented toward the AUT center, i.e., with the AUT center being the boresight direction of each probe antenna.

3.1.1. Basic principle

According to array theory, the complex conjugate of the array factor is equivalent to the beam steering factor associated with a given direction for a ULA. Consequently, adding more probes at properly designed locations as derived in [32] can be seen as virtually duplicating the beams steered by the AUT in the angular space. An example with an AUT steering 3 beams in the calibration measurement with a 1-probe setup and a 2-probe setup is illustrated in Fig. 3 (a) and 3 (b), respectively. For the single probe far-field setup, the corresponding weighting matrix is constructed based on the steering vectors of these 3 beams. When adding one more probe at location θ_m in the setup, 3 virtual beams are constructed via duplicating and shifting the 3 beams to location $-\theta_m$ as illustrated by Fig. 3 (b). Thus, the AUT steering 3 beams in the 2-probe setup in Fig. 3 (b) is equivalent to the AUT steering 6 beams in a 1-probe setup, where the 3 beams around $-\theta_m$ are attributed to the added probe. Accordingly, the virtual weighting matrix in an M-probe setup is composed of M blocks with the m-th block constructed based on the steering vectors of the virtual beams attributed to the m-th probe, i.e., the beams distributed around $-\theta_m$ as shown in Fig. 3 (b). The m-th block denoted by $\tilde{\mathbf{W}}_m$ is expressed as:

$$\tilde{\mathbf{W}}_m = \mathbf{W} \cdot \mathrm{diag}(\mathbf{a}_m), \tag{4}$$

where $\mathbf{W}$ is the actual weighting matrix implemented at the AUT, $\mathbf{a}_m \in \mathbb{C}^{N\times 1}$ denotes the array-factor vector associated with the m-th probe, and $\mathrm{diag}(\mathbf{x})$ represents a diagonal matrix with its diagonal elements given in the vector $\mathbf{x}$. By analogy, for an AUT steering beams to P directions in an M-probe setup, the achieved virtual weighting matrix $\tilde{\mathbf{W}} \in \mathbb{C}^{\tilde{P}\times N}$ can be constructed via simply stacking the M blocks. This virtual weighting matrix is equivalent to the weighting matrix

for the AUT steering beams to the $\tilde{P}$ directions in a single-probe setup, where $\tilde{P}$ denotes the number of virtual beam directions and we have $\tilde{P} = P \cdot M$. Accordingly, the received signal vector in the M-probe setup denoted by $\tilde{\mathbf{y}} \in \mathbb{C}^{\tilde{P}\times 1}$ can be formed via simply stacking the received signal vectors for sequentially activated probes. Once the virtual weighting matrix $\tilde{\mathbf{W}}$ has been constructed and the signal vector $\tilde{\mathbf{y}}$ has been measured, the calibration vector $\mathbf{c}$ can be calculated via operating pseudo inverse in (1) with $\mathbf{W}$ and $\mathbf{y}$ replaced by $\tilde{\mathbf{W}}$ and $\tilde{\mathbf{y}}$, respectively.

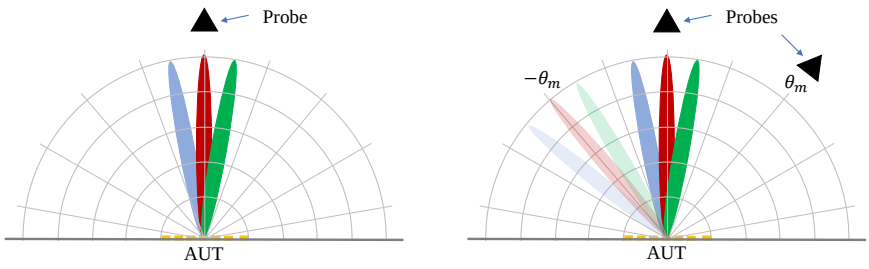

Fig. 3. An illustration of the duplication of beams due to multi-probes: the single-probe case (a) and the multi-probe case (b).

3.1.2. Discussion

The calibration errors in a multi-probe far-field setup are mainly introduced by the phase implementation errors in $\mathbf{W}$ in (4), the noise in $\mathbf{y}$ in (1), and the approximation errors in array factor vector $\mathbf{a}_m$ in (4) caused by the radiation patterns of DUT antennas and the probe antennas. As explained in [28], the condition number of the virtual weighting matrix $\tilde{\mathbf{W}}$ in (4) serves as an amplification factor of the first two error sources. Hence, the matrix $\tilde{\mathbf{W}}$ should be designed to have a condition number as small as possible, which can be achieved via widening beam-steering range $\bar{\Phi}$. To achieve this with a multi-probe setup, the edged probes should be located further away from the boresight direction, i.e., 0^O, which, however, will introduce larger approximation errors in array factor vector $\mathbf{a}_m$ in (4) as DUT antennas and probe antennas are typically not isotropic. Therefore, the optimization of the probe locations is a trade-off between the virtual beam-steering range $\bar{\Phi}$ (determining the condition number of matrix $\tilde{\mathbf{W}}$) and the approximation errors in array factor vector $\mathbf{a}_m$ caused by the radiation patterns of DUT antennas and the probe antennas.

To calibrate a ULA with a limited steering angular range, e.g., within $[-\Phi_P, \Phi_P]$, the probes should be distributed sparsely along the circle with the m-th probe positioned in the angular location $2\Phi_P \cdot (-\frac{M-1}{2} + m)$. The sparse setup can virtually widen the beam-steering angular range and thereby improve the calibration accuracy. While the dense-multi-probe setup can be used for ULAs with sparse beam directions, namely, with a large angular interval between the adjacent beams denoted by $\Delta\phi$. The M probe antennas are approximately uniformly distributed within the angular range $(-\Delta\phi/2, \Delta\phi/2)$. In an M-probe setup, whether dense or sparse, the number of necessary phase settings is decreased to $1/M$ of what a single-probe setup requires, signifying an improvement in measurement efficiency.

However, the multi-probe far-field scheme is limited for the ULA-type AUT in this paper, where a virtual DFT based weighting matrix can be constructed via properly designing the beam-steering matrix and the locations of the probes. For a non-ULA-type AUT calibrated in its beam-steering mode, the weighting matrix (not necessarily to be DFT based) should be optimized based on the beam-steering vectors, although the best condition matrix cannot always be guaranteed. However, the proposed multi-probe concept to enhance the calibration accuracy and improve the measurement efficiency should still work to a great extent.

3.2. Multi-probe near-field setup

As explained, for the DFF setup with a single-probe, the probe antenna should be placed in the far-field of the AUT, leading to a large and costly measurement setup. As the measurement distance gets smaller, the direct paths between the probe and the AUT elements might not propagate along the boresight direction of either the probe or these AUT elements any more. Consequently, the received signal vector differs from (1) and hence the estimated calibration vector will have larger errors as R decreases, due to the impact of radiation patterns of the AUT elements and the probe antenna. In order to calibrate arrays in a compact setup, a multi-probe setup is proposed in [30]. The basic idea is to employ the multiple probes to capture the scaled radiation pattern samples of each individual AUT element and then to perform the interpolation based on the samples of each AUT element for retrieving the boresight sample of the corresponding element.

3.2.1. Basic principle

As detailed in [30], the s-parameter between the n-th AUT antenna port and the m-th probe antenna port $s_{n,m}$ can be calculated via performing the pseudo inverse of the user-specified weighting matrix $\mathbf{W}$, which yields:

$$s_{n,m} = \tilde{c}_n \cdot g_{n,m} \cdot a_{n,m} \cdot \tilde{g}_{n,m}, \tag{5}$$

where $g_{n,m}$ is the antenna pattern of the n-th AUT element in the direction of the m-th probe, $a_{n,m}$ represents the free-space propagation coefficient between the n-th AUT element and the m-th probe, and $\tilde{g}_{n,m}$ denotes the radiation pattern of the m-th probe antenna in the direction of the n-th AUT element. Since the free-space propagation coefficients $a_{n,m}$ can be calculated according to the locations of the probes and the AUT elements, and the probe antenna patterns $\tilde{g}_{n,m}$ can be measured in advance, the last two terms in (5) are often known in practice and thereby the product of the first two terms can be obtained as $u_{n,m} = \tilde{c}_n \cdot g_{n,m}$. An interpolation process can then be implemented based on the M samples, i.e., $u_{n,m}$ with $m \in [1, M]$, to reconstruct the boresight sample of the n-th AUT element as illustrated by Fig. 4, where the retrieved boresight sample gives the estimated calibration coefficient of this element, i.e.,

$$\hat{c}_n = \tilde{c}_n \cdot \hat{g}_n^o, \tag{6}$$

with $\hat{g}_n^o$ denoting the retrieved boresight pattern of the n-th AUT element. The same interpolation process is implemented for each AUT element to obtain the calibration coefficient vector $\hat{\mathbf{c}}$.

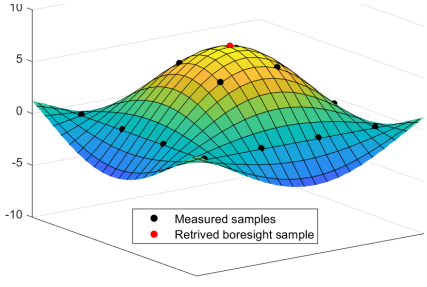

Fig. 4. An illustration of the interpolation.

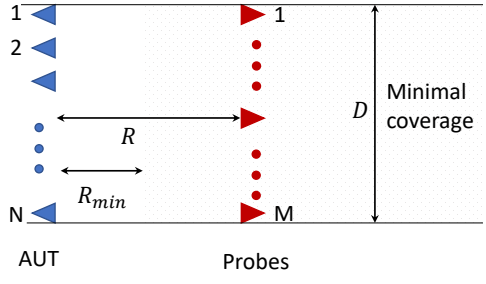

Fig. 5. Probe location design principle [30].

3.2.2. Discussion

In a multi-probe near-field setup, the calibration errors are mainly caused by the implementation errors in the phase setting matrix $\mathbf{W}$, the noise in the received signal $\mathbf{Y}$, and the interpolation errors in the retrieved boresight samples. The errors introduced by the former two sources can be well bounded if the phase setting matrix is properly designed to minimize its condition number. While the interpolation errors are determined by the density of pattern samples for a given DUT element, where more sparsely distributed pattern samples will result in larger interpolation errors.

Compared to the single-probe setup, which demands a far-field measurement range of the AUT array, a multi-probe near-field setup can significantly reduce the measurement range to fulfill just the far-field distance of the individual AUT elements. This distance is much smaller than that of the entire AUT array, making it especially useful for large aperture AUTs at mmWave frequencies. Furthermore, the unique advantage of this concept is that the measurement range is solely determined by the AUT elements, consequently not necessarily scaling with the dimensions of the AUT. In principle, the probe array should be designed to encompass the boresight direction patterns of all AUT elements to avoid extrapolation of element patterns, as extrapolation generally introduces greater errors compared to interpolation. Taking a ULA with an aperture of D as the AUT, two probes are firstly placed face-to-face with the two edged elements of the AUT and the rest probes are then evenly distributed in between, as illustrated by Fig. 5. As derived in [30], the minimum number of probes to calibrate an N-element AUT with an aperture of D at a measurement distance R can be calculated as:

$$M_{min} = \min\left\{\left\lceil \frac{D}{2R\tan(\frac{\Omega_{3dB}}{4})} + 1 \right\rceil, N\right\}, \tag{7}$$

where $\lceil\cdot\rceil$ denotes the rounding up operator and Ω_{3dB} represents the half-power beam width (HPBW) of the AUT elements.To calibrate an AUT with a given aperture, more probes are required when the measurement distance is reduced and/or the AUT elements become more directional. In practice, a few probe antennas should be sufficient for AUT element pattern interpolation, as the array elements are often not directional in design to cover a large beam-steering range. However, the multi-probe near-field setup requires the knowledge of the AUT configuration and probe antenna patterns, both of which should be compensated before the interpolation as explained.

4. Measurement validations

In this work, several new measurement campaigns were carried out in the anechoic chambers to validate the multi-probe concept for different objectives as detailed below.

4.1. Multi-probe scheme for improving measurement efficiency

As discussed, the multi-probe framework can be employed to improve the measurement efficiency compared to the single-probe framework, while maintaining calibration accuracy (guaranteed by the low condition number of the constructed virtual weighting matrix with a DFT structure). To experimentally validate it, a multi-probe far-field measurement setup implemented by a multi-feed CATR setup with offset-focus multiple feeds was utilized. The employed CATR system consists of nine feeds, which can generate plane waves with nine incident angles (with a 3^o interval) at the quiet zone. In our measurement, two plane waves (i.e. mimicking two far-field probes on the Rx side), with incident angles of 0^o and 6^o were generated by the multi-feed CATR setup. A quiet zone size of 36 cm (width) $\times$ 36 cm (height) can be supported with the CATR. A ULA composed of eight open-ended waveguide antennas with an element spacing of 28.76 mm and operating at 24.95 GHz was employed as the AUT. Note that only the odd AUT elements (i.e. 4 in total) were connected to 2-bit digital phase shifters with a phase adjustment range of 360^o and programmable attenuators. The measurement photo is shown in Fig. 6. More details about the multi-feed design can be found in [41], where the two feeds highlighted by the dashed boxes in Fig. 6 were used in the measurement after calibration.

4.1.1. Reference "probe and park" on-off measurement

The probe antenna was successively attached to each of the AUT element "face-to-face" and aligned, where only the attached AUT element was activated via setting 0 dB and 0^o and the rest of the elements were deactivated via setting 60 dB attenuation in the associated links. The measured calibration coefficients were used as the reference, i.e., the ground truth.

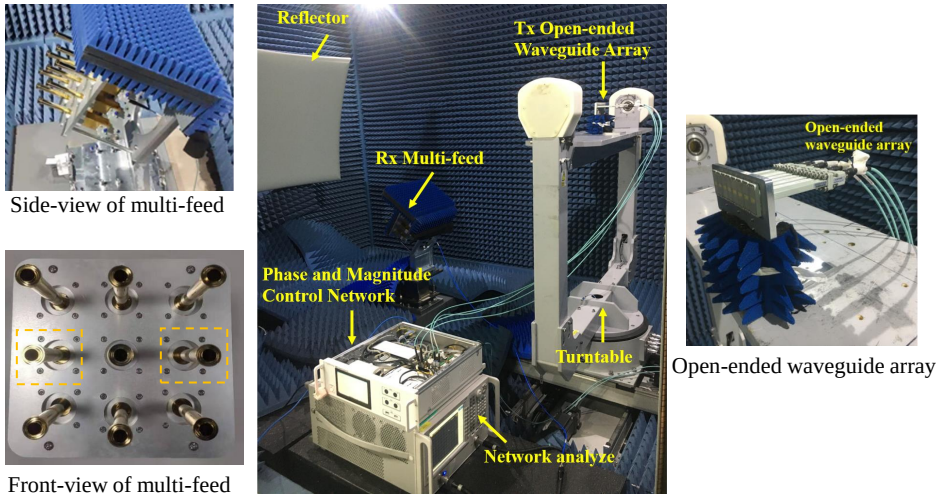

Fig. 6. Photographs of the multi-feed CATR calibration setup.

4.1.2. Hadamard matrix based measurement

A single Rx feed (which mimics a far-field probe in direction 0^o) was activated and the phase setting matrix was designed according to the Hadamard matrix [27]. Therefore, 4 measurement data were recorded, corresponding to 4 sets of phase shifter settings in the Hadamard matrix.

4.1.3. multi-probe algorithm implemented with the two-feed CATR system

The two-probe setup was realized by two Rx feeds. Two sets of phase shifter settings defined in (2) were successively implemented at the AUT element ports. For each set of phase shifter setting, the composite signals were recorded by the individual Rx antennas. Hence, 2 measurement data (one received at each Rx feed) for each set of phase shifter setting were recorded.

A high calibration accuracy can be achieved in general for both measurements, with ± 0.7 dB amplitude and $\pm 4^o$ phase errors compared to the reference measurement, respectively. The errors are mainly introduced by the phase shifter uncertainties, according to the datasheet specification of the phase shifters. Based on the validation results, one can conclude that high accuracy can be achieved, while the proposed multi-probe method can halve the number of required measurements (i.e. phase shifter settings), compared to the single-probe approach.

4.2. Multi-probe scheme for improving measurement accuracy

As discussed, the multi-probe framework can be employed to improve the measurement accuracy for phase arrays with limited beam-steering angular range, by virtually broadening the beam-steering range. The measurement setup was detailed in [32] and only outlined here.

The validation measurements were performed in a standard CATR setup, where a 4×4 mmWave phased array was employed as the AUT, as shown in Fig. 7. The calibration coefficients of the 1×4 ULA elements can be determined based on horizontal beam-steering measurements, with each ULA element being a subarray composed of 4×1 antenna elements. The AUT was placed in the quiet zone of the CATR. To validate the efficiency of the multi-probe calibration method in practice, we carried out two measurements, namely, the REV method to obtain the ground truth coefficients of the antenna-in-package (AiP) elements and the proposed multi-probe calibration method. The AUT was horizontally rotated around the azimuth axis from 90^o to -90^o with a step of -10^o, which is equivalent to multiple probes located in corresponding directions as shown in Fig. 7. For each orientation of the AiP (i.e. each probe location), the AiP performed horizontal beam-steering operations from -79.2^o to 79.2^o with a total of 65 beam-steering angles.

Note that the probe antennas should be placed properly in the multi-probe setup to well balance the reduction of the condition number and good approximation of the AUT element radiation

pattern. A large probe angular aperture though helpful in reducing the condition number, might lead to large element pattern approximation errors. A three-probe configuration with two side probes located at $\pm 30^o$ is adopted here.

The root-mean-square deviation (RMSD) was introduced as a figure of merit to evaluate the calibration accuracy as defined in [32]. The RMSD results achieved with the 3-probe setup (with the probes located at -30^o, 0^o and 30^o of the AUT) are compared with those obtained with the single-probe setup (with the probe located at 0^o), when the AUT steering beams within various angular ranges, as depicted in Fig. 8. As demonstrated by the blue dotted line, we can clear see that the array calibration accuracy is significantly affected by the beam-steering angle range, since a small angle-steering range would lead to a large condition number of the weighting matrix. The proposed 3-probe setup (illustrated by the red crossed line) can obviously improve the measurement accuracy compared to the single-probe setup (illustrated by the blue dotted line), especially when beam-steering ranges are small. The measurement results demonstrate the performance improvement with the proposed multi-probe method.

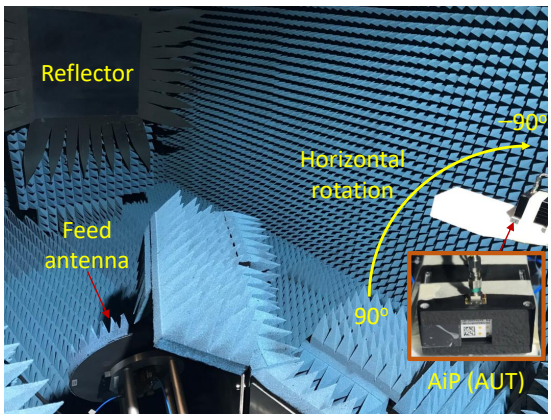

Fig. 7. A photo of the measurement setup seen inside the CATR chamber (VNA and control computer are outside the chamber and not shown) [32].

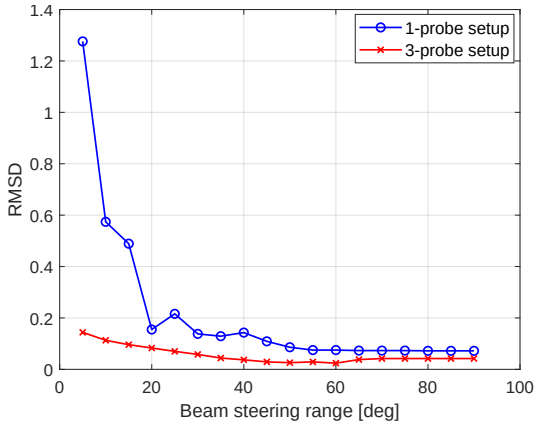

Fig. 8. Comparison of the calibration results with the DFT matrix-based method for various settings, with the REV method as the reference [35].

4.3. Multi-probe scheme for reducing measurement distance

As discussed, the multi-probe framework can be adopted to reduce the measurement range. The multi-probe concept was validated for a ULA composed of 14 elements in [30]. In this work, the concept was validated for a 2D rectangular array in an anechoic chamber with an even smaller measurement distance in Beihang University, China, as detailed below.

The measurement setup is illustrated by a photograph in Fig. 9, where a 14×9 non-uniform planar array (with a dimension of 1.124 m $\times$ 1 m) was employed as the AUT, with an operating frequency of 2.6 GHz. The far-field distance of the AUT can thereby be calculated according to the Fraunhofer distance $D_{ff} = 2D^2/\lambda = 2(1.124^2 + 1^2)/0.1154 = 39.2$ m. This distance cannot be accommodated in most anechoic chambers. The AUT elements are single-polarized open-ended waveguide antennas. Three 32-channel amplitude and phase control network units, each of which composes of a power splitting network, 8-digit programmable phase shifters and a 9-digit attenuators, were connected to the AUT elements.

The probe antenna is a standard waveguide WR284 with a typical gain of 5.6 dBi at 2.6 GHz and HPBW of around 71^o in the H plane and 127^o in the E plane, respectively. The probe antenna was attached on a 2D planar scanner, which supports scanning area of 2 m (in the y axis) $\times$ 3 m (in the x axis) with a step resolution of 0.1 mm. The probe antenna is moved to form a 10 $\times$ 10 virtual uniform rectangular array (URA) with the same aperture as the AUT in the measurement.

Fig. 9. A photo of the measurement setup of the multi-probe near-field scheme.

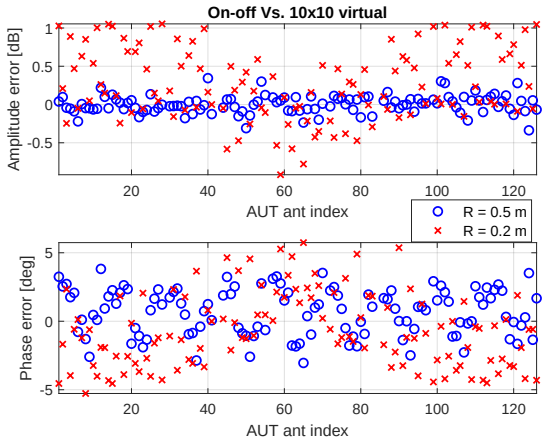

Fig. 10. Calibration results of the 10×10-probe setup with the measurement distance set to 0.5 m and 0.2 m, respectively.

Two measurement distances, i.e., 0.5 m and 0.2 m, were adopted for the multi-probe validation measurements, respectively. For simplicity, the transfer matrix between the AUT antenna elements and the probe antennas was recorded using the on-off mode with the VNA.

The on-off measurement with a measurement distance at 0.5 m was performed and selected as the reference measurement to validate the multi-probe concept. The calibration results with the 10×10-probe setup at 0.5 m and 0.2 m are presented by blue dots and red crosses in Fig. 10, respectively. The measurement results demonstrate that:

- Good accuracy can be achieved for both of the measurements at distance of 0.5 m (with amplitude errors up to ±0.3 dB and phase errors up to $\pm3^o$, respectively), and 0.2 m (with amplitude errors up to ±1 dB and phase errors up to $\pm6^o$, respectively). Compared to the required far-field distance of 39.2 m for a single-probe antenna setup, the proposed multi-probe framework can significantly reduce the measurement distance while maintaining a good accuracy.
- The calibration accuracy achieved at $R = 0.2$ m was worse than that at $R = 0.5$ m, mainly due to the fact that 1) a given probe array configuration at a smaller distance covers a larger angular space of each AUT element, resulting in a larger interpolation errors; 2) the complex-signal measurements are less reliable due to high attenuation introduced by AUT element pattern effects, especially for the elements at the edge of the AUT; 3) more severe coupling presents between the probe antenna and the AUT.

5. Conclusion

Phased array calibration is crucial to guarantee that their radiation performance aligns with the standard requirements prior to a widespread deployment. This paper introduces a multi-probe framework to tackle the challenges associated with phased array calibration. Three multi-probe schemes are presented for different objectives, i.e., speeding up calibration measurement, enhancing calibration accuracy and reducing measurement distance, respectively. For each scheme, the basic principle and probe configuration are described in detailed whereas the pros and cons are clearly stated. In addition, extensive measurements were conducted in anechoic chambers for calibrating different AUTs. For the efficiency improvement measurement, it was demonstrated that the number of required measurements with a two-probe setup can be halved compared to the single-probe setup, with amplitude errors of up to ±0.7 dB and phase errors of up to ±0.4, respectively. For the accuracy enhancement measurement, one demonstrated that a three-

TABLE I
Comparison of calibration methods in single-probe and multi-probe setups.

Setup	Measurement range	Data type	Method	Minimum number of measurements	Minimum phase shifter bits	Measurement accuracy
Single -probe	Far-field	Complex-signal	Hadamard matrix	N	1	Error sources include phase shifter uncertainties and noise. Robust for various N.
			DFT matrix	N	$\log_2 N$	
		Amplitude-only	REV	$(Q-1)N+1$	$\log_2 Q$	Error sources include phase shifter uncertainties and noise. More sensitive to noise for a larger N. More phase tuning states Q can help achieve a higher accuracy.
			Fast amplitude-only	$2N+1$	2	
Multi-probe	Far-field	Complex-signal	DFT matrix	N/M	$\log_2 N$ for probes with large intervals. $\log_2(N/M)$ for probes with small intervals.	Error sources include phase shifter uncertainties, noise, probe location errors and non-uniformity among probes. Robust for various N. Limited to ULAs.
	Near-field	Complex-signal	Hadamard matrix	N	1	Error sources include phase shifter uncertainties, noise, probe location errors, non-uniformity among probes and interpolation errors. Robust for various N.
			DFT matrix	N	$\log_2 N$	

probe setup can significantly reduce the calibration error, compared to a single-probe setup, especially when the beam-steering angle range is limited. For the measurement range reduction measurement, one demonstrated that the distance can be reduced from the required 39.2 m for the single probe setup to as small as 0.5 m with the employment of a 10 $\times$ 10 virtual probe array setup, which can achieve amplitude errors up to ± 0.3 dB and phase errors up to $\pm 3^o$, respectively. The comparison of various calibration methods in both single-probe and multi-probe setups is summarized in Table I.

The multi-probe scheme is highly promising for testing future advanced mmWave radios. There are some logic extensions for current works. For example, power-only based methods will be of more importance at mmWave bands, due to inaccessible or inaccurate phase measurement. The multi-probe scheme discussed in this paper works only for complex-signal based measurements, while it cannot be directly applied for power-only based measurements. It would be of high interest to extend the multi-probe concept for power-only measurements.

6. acknowledgement

This work was supported in part by the start-up Research Fund of Southeast University, China, under Project RF1028623309; The work of AAU and NPL was supported by the EURAMET European Partnership on Metrology (EPM), under 21NRM03 Metrology for Emerging Wireless Standards (MEWS) project.

Biographies

F. Zhang (fz@es.aau.dk) is currently an Assistant Professor with the Department of Electronics Systems, Aalborg University, Denmark. Her research interests are in antenna array signal processing, channel estimation, over the air testing of multiple antenna systems.

Z. Wang (wangzp@buaa.edu.cn) is with Beihang Univeristy, Beijing, China, 100191. His current research interests include over the air (OTA) test, reconfigurable antennas, compact antenna test range feed antenna, and antenna measurement.

T. Loh (tian.loh@npl.co.uk) is a Principal Scientist at the UK National Physical Laboratory (NPL), Teddington, Middlesex TW11 0LW, United Kingdom. His research interests include 5G/6G communications, smart antennas, small antennas, metamaterials, body-centric communications, integrated sensing and communication, electromagnetic compatibility, and computational electromagnetics.

Y. Gui (yunsong.gui@npl.co.uk) is with National Physical Laboratory(NPL), Teddington, Middlesex TW11 0LW, United Kingdom. His current research interests include the performance evaluation and verification of the wireless communication system, and wireless channel measurement and modelling.

S. Tang (tang_sii@163.com) is currently a EMC developer with Ericsson (China) Company Limited. She received the M.Sc degree from Beihang University, Beijing, China, in 2023. Her main research interests include phased array calibration and RF testing.

W. Fan (weifan@seu.edu.cn) is currently a Professor at National Mobile Communications Research Laboratory, School of Information Science and Engineering, Southeast University, Nanjing 210096, China. His research interests include over-the-air (OTA) testing of multiple antenna systems, radio channel sounding, parameter estimation, modeling, and emulation.

References

[1] Y. P. Zhang and D. Liu, "Antenna-on-chip and antenna-in-package solutions to highly integrated millimeter-wave devices for wireless communications," *IEEE transactions on antennas and propagation*, vol. 57, no. 10, pp. 2830–2841, 2009.

[2] S. Amakawa, Z. Aslam, J. Buckwater, S. Caputo, A. Chaoub, Y. Chen, Y. Corre, M. Fujishima, Y. Ganghua, S. Gao *et al.*, "White paper on RF enabling 6G–opportunities and challenges from technology to spectrum," 2021.

[3] H. Kong, Z. Wen, Y. Jing, and M. Yau, "Midfield over-the-air test: A new OTA RF performance test method for 5G massive MIMO devices," *IEEE Transactions on Microwave Theory and Techniques*, vol. 67, no. 7, pp. 2873–2883, 2019.

[4] Y. Qi, G. Yang, L. Liu, J. Fan, A. Orlandi, H. Kong, W. Yu, and Z. Yang, "5G over-the-air measurement challenges: overview," *IEEE Transactions on Electromagnetic Compatibility*, vol. 59, no. 6, pp. 1661–1670, 2017.

[5] M. Rumney, "Testing 5G: Time to throw away the cables," *Microw. J*, vol. 59, no. 11, pp. 10–18, 2016.

[6] P. Zhang, X. Yang, J. Chen, and Y. Huang, "A survey of testing for 5G: Solutions, opportunities, and challenges," *China Communications*, vol. 16, no. 1, pp. 69–85, 2019.

[7] F. Scattone, D. Sekuljica, A. Giacomini, F. Saccardi, A. Scannavini, L. Foged, E. Kaverine, S. Anwar, N. Gross, and P. Iversen, "Validation of millimeter-wave plane wave generator for 5G measurements," in *2021 Antenna Measurement Techniques Association Symposium (AMTA)*. IEEE, 2021, pp. 1–3.

[8] T. Loh, D. Cheadle, M. Khalily, S. Payami, K. Nikitopoulos, and R. Tafazolli, "A metrological millimeter wave hybrid beamforming testbed with a large antenna array," 2021.

[9] B. Yang, Z. Yu, J. Lan, R. Zhang, J. Zhou, and W. Hong, "Digital beamforming-based massive MIMO transceiver for 5G millimeter-wave communications," *IEEE Transactions on Microwave Theory and Techniques*, vol. 66, no. 7, pp. 3403–3418, 2018.

[10] S. Payami, M. Khalily, A. Araghi, T. H. Loh, D. Cheadle, K. Nikitopoulos, and R. Tafazolli, "Developing the first mmWave fully-connected hybrid beamformer with a large antenna array," *IEEE Access*, vol. 8, pp. 141 282–141 291, 2020.

[11] Y. Ji, J. Ø. Nielsen, and W. Fan, "A simultaneous wideband calibration for digital beamforming arrays at short distances [measurements corner]," *IEEE Antennas and Propagation Magazine*, vol. 63, no. 3, pp. 102–111, 2021.

[12] R. Sorace, "Phased array calibration," *IEEE Transactions on antennas and propagation*, vol. 49, no. 4, pp. 517–525, 2001.

[13] T. Takahashi, Y. Konishi, S. Makino, H. Ohmine, and H. Nakaguro, "Fast measurement technique for phased array calibration," *IEEE Transactions on Antennas and Propagation*, vol. 56, no. 7, pp. 1888–1899, 2008.

[14] F. Scattone, D. Sekuljica, A. Giacomini, F. Saccardi, A. Scannavini, N. Gross, E. Kaverine, P. Iversen, and L. Foged, "Design of dual polarised wide band plane wave generator for direct far-field testing," in *2019 13th European Conference on Antennas and Propagation (EuCAP)*. IEEE, 2019, pp. 1–4.

[15] M. Li, F. Zhang, Z. Wang, and W. Fan, "Fast array diagnosis for subarray structured 5G base station antennas," *IEEE Antennas and Wireless Propagation Letters*, vol. 21, no. 7, pp. 1393–1397, 2022.

[16] Z. Qiao, Z. Wang, and J. Miao, "A high channel consistency subarray of plane-wave generators for 5G base station OTA testing," *Electronics*, vol. 8, no. 10, p. 1148, 2019.

[17] D. Ulm, T. Kleine-Ostmann, and T. Schrader, "Antenna calibration based on near-field to far-field transformation algorithms," in *2019 13th European Conference on Antennas and Propagation (EuCAP)*. IEEE, 2019, pp. 1–4.

[18] L. Scialaequa, F. Scattone, A. Giacomini, L. Foged, and F. Mioc, "Advanced diagnostics on a large array by the equivalent current technique," in *2021 Antenna Measurement Techniques Association Symposium (AMTA)*. IEEE, 2021, pp. 1–5.
[19] J. E. Hansen, *Spherical near-field antenna measurements*. Iet, 1988, vol. 26.
[20] K. Hassett, "Phased array antenna calibration measurement techniques and methods," in *European Conference Antennas Propagation (EuCAP)*, 2016.
[21] L. Kuai, J. Chen, Z. H. Jiang, C. Yu, C. Guo, Y. Yu, H.-X. Zhou, and W. Hong, "A N260 band 64 channel millimeter wave full-digital multi-beam array for 5G massive MIMO applications," *IEEE Access*, vol. 8, pp. 47 640–47 653, 2020.
[22] H. Gao, W. Wang, Y. Wu, Y. Liu, G. F. Pedersen, and W. Fan, "Experimental comparison of on–off and all-on calibration modes for beam-steering performance of mmWave phased array antenna-in-package," *IEEE Transactions on Instrumentation and Measurement*, vol. 70, pp. 1–9, 2021.
[23] 3GPP TR 38.810, "NR; study on test methods (release 16)," V16.0.0 (2018-09).
[24] C. Rowell and A. Tankielun, "Plane wave converter for 5G massive MIMO basestation measurements," in *12th European Conference on Antennas and Propagation (EuCAP 2018)*. IET, 2018, pp. 1–3.
[25] Y. Zhang, Z. Wang, X. Sun, Z. Qiao, W. Fan, and J. Miao, "Design and implementation of a wideband dual-polarized plane wave generator with tapered feeding nonuniform array," *IEEE Antennas and Wireless Propagation Letters*, vol. 19, no. 11, pp. 1988–1992, 2020.
[26] F. Scattone, D. Sekuljica, A. Giacomini, F. Saccardi, A. Scannavini, E. Kaverine, S. Anwar, N. Gross, P. Iversen, and L. Foged, "Towards testing of 5G millimeter wave devices using plane wave generators," in *2021 15th European Conference on Antennas and Propagation (EuCAP)*. IEEE, 2021, pp. 1–4.
[27] R. Long, J. Ouyang, F. Yang, W. Han, and L. Zhou, "Multi-element phased array calibration method by solving linear equations," *IEEE Transactions on Antennas and Propagation*, vol. 65, no. 6, pp. 2931–2939, June 2017.
[28] Z. Wang, F. Zhang, H. Gao, O. Franek, G. F. Pedersen, and W. Fan, "Over-the-air array calibration of mmWave phased array in beam-steering mode based on measured complex signals," *IEEE Transactions on Antennas and Propagation*, pp. 1–1, 2021.
[29] R. Long, J. Ouyang, F. Yang, W. Han, and L. Zhou, "Fast amplitude-only measurement method for phased array calibration," *IEEE transactions on antennas and propagation*, vol. 65, no. 4, pp. 1815–1822, 2016.
[30] Y. Zhang, Z. Wang, F. Zhang, X. Chen, J. Miao, and W. Fan, "Phased array calibration based on measured complex signals in a compact multiprobe setup," *IEEE Antennas and Wireless Propagation Letters*, vol. 21, no. 4, pp. 833–837, 2022.
[31] S. Tang, Z. Wang, C. Pan, R. Su, W. Fan, and S. Gao, "A fast and efficient calibration method for phased array antennas using fourier-structured excitation matrix," *IEEE Transactions on Antennas and Propagation*, 2023.
[32] F. Zhang, H. Gao, Z. Wang, and W. Fan, "An improved complex signal based calibration method for beam-steering phased array," *IEEE Antennas and Wireless Propagation Letters*, pp. 1–1, 2021.
[33] H. Gao, W. Fan, W. Wang, F. Zhang, Z. Wang, Y. Wu, Y. Liu, and G. F. Pedersen, "On uncertainty investigation of mmWave phased-array element control with an all-on method," *IEEE Antennas and Wireless Propagation Letters*, vol. 19, no. 11, pp. 1993–1997, 2020.
[34] F. Zhang, W. Fan, Z. Wang, Y. Zhang, and G. F. Pedersen, "Improved over-the-air phased array calibration based on measured complex array signals," *IEEE Antennas and Wireless Propagation Letters*, vol. 18, no. 6, pp. 1174–1178, June 2019.
[35] T. Takahashi, Y. Konishi, and I. Chiba, "A novel amplitude-only measurement method to determine element fields in phased arrays," *IEEE Transactions on Antennas and Propagation*, vol. 60, no. 7, pp. 3222–3230, July 2012.
[36] R. E. Sorace, V. S. Reinhardt, and C. Chan, "Phase array calibration orthogonal phase sequence," 1999.
[37] H.-J. Yoon and B.-W. Min, "Improved rotating-element electric-field vector method for fast far-field phased array calibration," *IEEE Transactions on Antennas and Propagation*, vol. 69, no. 11, pp. 8021–8026, 2021.
[38] L. Zhu, F. Xu, X. Zhang, Z. Yu, J. Zhou, R. Lu, and W. Hong, "An efficient OTA calibration and pattern estimation method for 5G mmWave large-scale arrays," *IEEE Transactions on Antennas and Propagation*, vol. 70, no. 9, pp. 8440–8451, 2022.
[39] C. Rowell, A. C. Garcia, and B. Derat, "Active 5G radio resource management measurements using a multiple CATR reflector system," *International Journal of Microwave and Wireless Technologies*, pp. 1–7, 2022.
[40] J. Hakli, T. Koskinen, J. Ala-Laurinaho, and A. Raisanen, "Dual reflector feed system for hologram-based compact antenna test range," *IEEE transactions on antennas and propagation*, vol. 53, no. 12, pp. 3940–3948, 2005.
[41] Z. Ning, Z. Wang, and Z. Yu, "Design of a millimeter wave multi-feeds compact range," in *2020 IEEE MTT-S International Wireless Symposium (IWS)*. IEEE, 2020, pp. 1–3.